Fast scanning coaxial optoacoustic microscopy

Rui Ma, Sebastian Söntges, Shy Shoham, Vasilis Ntziachristos, and Daniel Razansky*

*Institute for Biological and Medical Imaging, Technical University of Munich and Helmholtz Center Munich,
Ingolstädter Landstraße 1, 85764 Neuherberg, Germany*

*dr@tum.de

Abstract: The hybrid nature of optoacoustic imaging might impose limitations on concurrent placement of optical and ultrasonic detection components, especially in high resolution microscopic applications that require dense arrangements and miniaturization of components. This hinders optimal deployment of the optical excitation and ultrasonic detection paths, leading to reduction of imaging speed and spatial resolution performance. We suggest a compact coaxial design for optoacoustic microscopy that allows optimizing both the light illumination and ultrasonic detection parameters of the imaging system. System performance is showcased in phantoms and *in vivo* imaging of microvasculature, achieving real time operation in two dimensions and penetration of 6 mm into optically dense human tissues.

OCIS codes: (170.5120) Photoacoustic imaging; (110.6880) Three-dimensional image acquisition; (170.3880) Medical and biological imaging; (120.3890) Medical optics instrumentation.

References and links

1. D. Razansky, M. Distel, C. Vinegoni, R. Ma, N. Perrimon, R. W. Köster, and V. Ntziachristos, "Multi-spectral optoacoustic tomography of deep-seated fluorescent proteins in-vivo," Nat. Photonics **3**(7), 412–417 (2009).
2. D. Razansky, A. Buehler, and V. Ntziachristos, "Volumetric real-time multispectral optoacoustic tomography of biomarkers," Nat. Protoc. **6**(8), 1121–1129 (2011).
3. J. Gamelin, A. Aguirre, A. Maurudis, F. Huang, D. Castillo, L. V. Wang, and Q. Zhu, "Curved array photoacoustic tomographic system for small animal imaging," J. Biomed. Opt. **13**(2), 024007 (2008).
4. L. Song, K. Maslov, K. K. Shung, and L. V. Wang, "Ultrasound-array-based real-time photoacoustic microscopy of human pulsatile dynamics *in vivo*," J. Biomed. Opt. **15**(2), 021303 (2010).
5. R. J. Zemp, L. Song, R. Bitton, K. K. Shung, and L. V. Wang, "Realtime photoacoustic microscopy of murine cardiovascular dynamics," Opt. Express **16**(22), 18551–18556 (2008).
6. H. F. Zhang, K. Maslov, and L. V. Wang, "*In vivo* imaging of subcutaneous structures using functional photoacoustic microscopy," Nat. Protoc. **2**(4), 797–804 (2007).
7. Z. Xie, S.-L. Chen, T. Ling, L. J. Guo, P. L. Carson, and X. Wang, "Pure optical photoacoustic microscopy," Opt. Express **19**(10), 9027–9034 (2011).
8. E. Z. Zhang, J. G. Laufer, R. B. Pedley, and P. C. Beard, "*In vivo* high-resolution 3D photoacoustic imaging of superficial vascular anatomy," Phys. Med. Biol. **54**(4), 1035–1046 (2009).
9. L. Wang, K. Maslov, J. Yao, B. Rao, and L. V. Wang, "Fast voice-coil scanning optical-resolution photoacoustic microscopy," Opt. Lett. **36**(2), 139–141 (2011).
10. Z. Xie, S. Jiao, H. F. Zhang, and C. A. Puliafito, "Laser-scanning optical-resolution photoacoustic microscopy," Opt. Lett. **34**(12), 1771–1773 (2009).
11. C. Zhang, K. Maslov, S. Hu, R. Chen, Q. Zhou, K. K. Shung, and L. V. Wang, "Reflection-mode submicron-resolution *in vivo* photoacoustic microscopy," J. Biomed. Opt. **17**(2), 020501 (2012).
12. M. L. Li, H. E. Zhang, K. Maslov, G. Stoica, and L. V. Wang, "Improved *in vivo* photoacoustic microscopy based on a virtual-detector concept," Opt. Lett. **31**(4), 474–476 (2006).
13. C. P. Favazza, L. A. Cornelius, and L. V. Wang, "*In vivo* functional photoacoustic microscopy of cutaneous microvasculature in human skin," J. Biomed. Opt. **16**(2), 026004 (2011).
14. E. W. Stein, K. Maslov, and L. V. Wang, "Noninvasive, *in vivo* imaging of blood-oxygenation dynamics within the mouse brain using photoacoustic microscopy," J. Biomed. Opt. **14**(2), 020502 (2009).
15. M. Cutolo, A. Sulli, M. E. Secchi, S. Paolino, and C. Pizzorni, "Nailfold capillaroscopy is useful for the diagnosis and follow-up of autoimmune rheumatic diseases. a future tool for the analysis of microvascular heart involvement?" Rheumatol. **45**(Supplement 4), 43–46 (2006).
16. P.-C. Wu, M.-N. Huang, S.-C. Hsieh, and C.-L. Yu, "Diagnostic value of nailfold capillaroscopy to systemic sclerosis with Raynaud's phenomenon: a preliminary study," Formosan J. Rheumatol. **23**, 37–42 (2009).

1. Introduction

Optoacoustic imaging is based on detection of acoustic waves generated by absorption of short pulsed light beams in tissues. Due to its hybrid nature, it combines the advantages of both optical and ultrasound imaging, i.e. high light-based contrast and diffraction-limited ultrasonic resolution in deep tissues independent from photon scattering. There are two major types of optoacoustic systems based on either tomographic reconstruction [1–5] or linear scanning of point detectors or focused elements, which is mainly employed in microscopic systems [6,7]. In order to increase the imaging speed, multi-element transducer arrays can generally be used, which are able to simultaneously detect optoacoustic responses at multiple locations [2,5]. This option is however difficult to implement for high resolution microscopic applications, which require high frequency detection technology operational at 50Mhz and beyond. Therefore most microscopic systems opt for single spherically-focused ultrasonic detectors [6] or utilize pure optical point detection approaches using resonators [7] or interferometric approaches [8].

Optoacoustic microscopy systems can be generally divided into two main categories. Optical resolution photoacoustic microscopy (OR-PAM) utilizes high numerical aperture (NA) objective in order to create diffraction-limited optical focus on the tissue surface, while the optoacoustic responses are subsequently detected by an unfocused ultrasonic transducer [9,10]. To this end, OR-PAM has achieved 220 nm lateral resolution and made it possible to resolve subcellular organelles. Yet, since the image formation purely relies on the optical focus, when the target object is located outside the focal zone, imaging resolution degrades dramatically (e.g. 0.1 mm off the focus the beam size might expand to 0.1 mm and more). It is also possible to gain axial (depth) resolution from the time axis of signals detected by the transducer [11]. However, the spatial resolution of OR-PAM is directly affected by light scattering, which limits its applicable imaging depth to about 1mm or less in most tissues.

To image deeper in tissues, photoacoustic microscopy (PAM) that purely relies on the acoustic resolution, is employed. In its classical dark-field illumination form, a spherically-focused ultrasonic detector is used while the illuminating light is guided around the detector with concave mirrors. In this way, for transducer with central frequency of 50Mhz, diffraction-limited ultrasonic resolution of 15 µm (axially) and 45 µm (laterally) can be reached in the transducer focus [6]. Using virtual detector approach, similar resolution can also be achieved beyond the focal point [12]. PAM has been broadly applied to skin vasculature imaging [13] and noninvasive imaging of mouse brain [14], however, is characterized by long acquisition times and is generally not suitable for real time imaging of dynamic processes. This is because optimization of the optoacoustic signal intensity implies maximal possible confinement of the illuminating light to the focal zone (line) of the ultrasonic detector. The major technical limitation arises from the need of coaxial placement of optical illumination and ultrasonic detection paths. This turns challenging when tight acoustic focusing with high numerical aperture transducer, placed in close vicinity of the sample, is used for attaining superior imaging resolution. In the dark-field arrangement, a relatively broad and suboptimal (ring-type) light pattern is therefore created in the object, which leads to low light fluence in the focal zone of the transducer and an overall loss of the signal-to-noise ratio (SNR), imaging speed and/or penetration depth.

Herein we present a compact real-time optoacoustic microscope design with the excitation light guided through the transducer aperture, which allows for optimal deployment of the optical excitation and ultrasonic detection paths. Real time image acquisition is further facilitated by the use of a fast scanning linear stage.

2. Experimental setup

A simplified sketch of the experimental setup is shown in Fig. 1. The optoacoustic microscope employs a saw-tooth scan motion, where real time two-dimensional (2D) scans are enabled by

a high speed linear stage M-683.2U4 controlled by a C-867.160 Piezomotor Controller (Physik Instrumente GmbH & Co., Karlsruhe, Germany) while an additional motorized linear stage (LTM 60F, OWIS GmbH, Staufen, Germany) is used to obtain three-dimensional (3D) data. We use a passively Q-switched solid state diode pumped laser (Flare PQ HP GR, InnoLight GmbH, Hannover, Germany), operating at 515nm, as the excitation source for generation of optoacoustic signals. It delivers < 3 ns duration pulses with an average per-pulse energy of 0.5mJ at 1.5 kHz pulse repetition rate. Small portion of the beam is reflected by an uncoated broadband precision window (WG10530, Thorlabs, Dachau, Germany) and detected by a photodiode (FDS010, 200-1100 nm, 1 ns rise time, Thorlabs, Dachau, Germany) used for pulse calibration and triggering of data acquisition. The rest of the output energy is coupled to a multi-mode (MM) fiber (M29L05, 600 µm core diameter, 0.39 NA, Thorlabs, Dachau, Germany). The distal side of the MM fiber is cleaved and inserted through a 1mm diameter hole in a customized PZT ultrasound transducer with a central frequency of 50 MHz, 67% bandwidth, focal length of 7.15 mm and element diameter of 6 mm (InSensor, Denmark). The fiber input is fixed to a lens tube for fine adjustment of the light fluence delivered to the tissue.
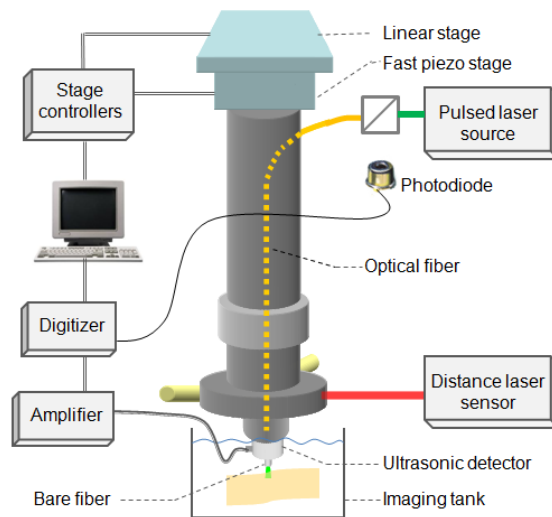

Fig. 1. Illustration of the fast scanning coaxial optoacoustic microscope.

Since the laser is passively Q-switched, the time interval between adjacent pulses varies significantly. The peak-to-peak instability is 10.4% and the standard deviation of pulse-to-pulse jitter is 41.4 µs with an average pulse period of 630.9 µs, which indicates 6.6% of timing jitter instability. The pulse-to-pulse jitter can reach up to 100 µs, which is ~16% of the pulse period. In order to avoid uncertainty of scan positions for each trigger event, we choose a laser distance sensor M11L/10-10B (MEL Mikroelektronik GmbH, Eching, Germany), providing an analog output representing the scan position, to measure the position of the transducer in real-time. The sensor has a total measurement range of 10 mm with 2.5 µm resolution and up to 10 kHz sampling rate. The ultrasound signals detected by the transducer and the corresponding positions of the piezo stage are acquired by a UF3-4142 PCI Express card (Strategic Test AB, Sweden). The digitizer has a 128 MSample (256 Mbyte) memory and a 14-bit resolution. The sampling rate of the digitizer is 250 MS/s when both of its channels are used simultaneously.

3. Phantom experiments

For testing spatial resolution of the system, a pure agar phantom embedded with 10 µm black-dyed polystyrene microspheres (Polysciences, Inc., Warrington, PA) was prepared. Figure 2(a) shows the optoacoustic image of this sphere placed at the focal point of the transducer. Lateral and axial resolutions were quantified at 50 µm and 11 µm, respectively.

Spatial resolutions were estimated by calculating the value of $\sqrt{FWHM^2 - D^2}$, where FWHM is the full-width-half-maximum of the horizontal or vertical cuts through the optoacoustic image and D is diameter of the microsphere.
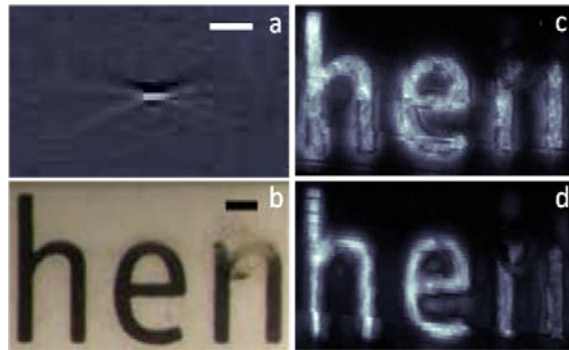

Fig. 2. (a) Calibration of the system resolution at the focal point of a spherically focused transducer (50 MHz center frequency) using a 10 µm black-dyed polystyrene microsphere. Scale bar corresponds to 100 µm; (b) Photograph of the imaged printed letters; (c) Raw MAP optoacoustic image of the letters; (d) The MAP image corrected using the SAFT method. Scale bar in (b)-(d) corresponds to 500 µm.

To further optimize lateral imaging performance of the system, we imaged printed letters as shown in Fig. 2(b), placed slightly away from the focal zone of the transducer. The lateral scan range of each 2D optoacoustic image is 5 x 4.5 mm with 20 µm step size for adjacent scan lines. In total, 91 frames with 50 µm distance between neighboring frames were acquired. Figure 2(c) shows the maximum amplitude projection (MAP) of the 3D reconstructed optoacoustic image. The MAP represents well the overall shape and size of the printed letters as compared with the photograph with some out-of-focus artifacts. We subsequently applied a virtual-detector-based synthetic-aperture focusing technique (SAFT) [12] to improve the lateral resolution outside the focal zone of the spherically focused transducer. Figure 2(d) shows the corrected image, in which the out-of-focus artifacts have been significantly reduced. In the current implementation, the light beam diameter was relatively large, thus, the effective lateral window of the SAFT algorithm was much smaller compared to the width of the illuminating beam. Nevertheless, future implementations that seek to increase the laser fluence by reducing the beam diameter should indeed consider effects of spatial light distribution in the imaged volume for the SAFT reconstructions.

The real-time imaging capability of the system has been verified using chicken tissue, in which a polythene tube (ID 0.28 mm, OD 0.61mm, Smiths Medical Deutschland GmbH, Grasbrunn, Germany) was inserted. The tube was inserted into the chicken specimen and filled with ink containing air bubbles. At one end of the tube a syringe filled with India ink solution was connected for injection. We imaged ink flow through the polythene tube with a frame rate of 5 frames/s and a scan range of 4 mm. These parameters were mainly dictated by the 1.5 kHz repetition rate of the laser. We monitored ink injection in real time over 10 consecutive seconds (see Fig. 3 and Media 1), attaining good contrast without signal averaging.
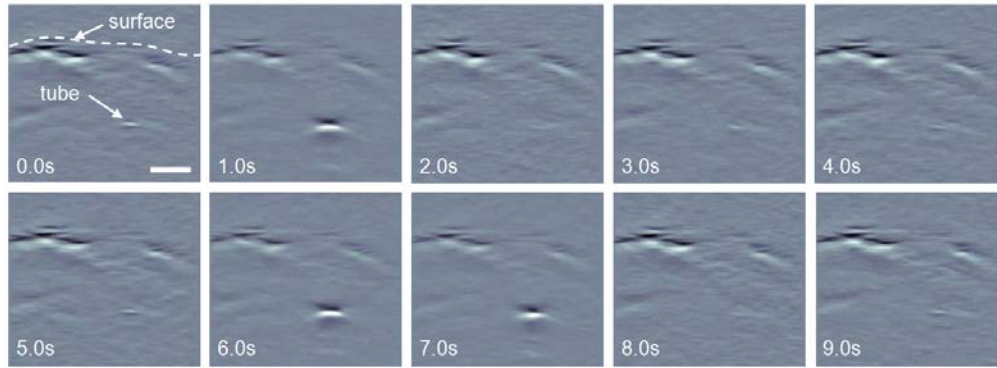
Fig. 3. (Media 1) Real-time monitoring of ink injection through a tube embedded into chicken phantom. Scale bar: 2 mm.

4. *Ex vivo* mouse imaging

Images acquired from a white mouse post mortem are shown in Fig. 4. In this case, a single 2D frame was created every 1 sec while lateral field of view of 8 x 18 mm was covered by acquiring 1200 adjacent frames with 15 µm step size. Figure 4(a) shows the raw maximum amplitude projection (MAP) image. The out-of-focus imaging quality was subsequently improved by applying the SAFT, as shown in Fig. 4(b). The black arrows point at blood vessels that do not show in the original image while blue arrows point at places where image quality improves after applying the SAFT. Clearly, this correction algorithm is not able to improve image quality beyond the diffraction limit of the ultrasonic detector. Therefore, no improvements are visible in the focal area of the detector whereas additional smearing affects appeared around the focus after applying SAFT, presumably due to high sensitivity of the algorithm to noise in the focal area. To restore fine details in this area, we combined images before and after applying the SAFT, as shown in Fig. 4(c).
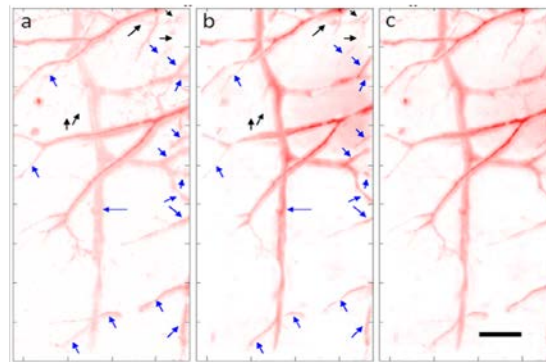

Fig. 4. Imaging of white mouse *post mortem* in the breast area. Total field of view: 8 mm X 18 mm. (a) Raw MAP optoacosutic image; (b) MAP after applying the SAFT; (c) Combination of (a) and (b). Black arrows point at blood vessels that do not show in the raw image and blue arrows point at places where image quality improves after applying SAFT. Scale bar corresponds to 2 mm.
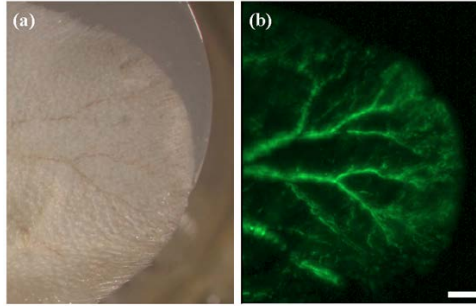
Fig. 5. Imaging of a fixed mouse ear embedded in agar. Total (a) A color photograph of the ear; (b) MAP of the 3D reconstructed optoacoustic image of mouse ear. Scale bar: 1 mm. 3D rendering can be found in Media 2.

Three-dimensional visualization capacity of the system is demonstrated by imaging a formalin-fixed mouse ear embedded in pure agar phantom. The total lateral field of view in this case is 8 x 10 mm with 756 adjacent slices acquired at 0.75 frame/s. Figure 5 shows a picture and MAP optoacoustic image of the ear. 3D rendering can be found in Media 2.

5. Microscopic human imaging

In order to assess the system's ability to penetrate into human tissues, imaging of an author's palm was performed using settings similar to the mouse experiments. A typical frame, which is shown in Fig. 6(a), was acquired from an area as marked in Fig. 6(b). Blood vessels up to a depth of approximately 3.2 mm are clearly distinguishable in the optoacoustic image.

The corresponding 3D data set was next acquired at a 2D frame rate of 1.1 frames/s with a total lateral field of view of 8 x 8 mm, as marked in Fig. 6(b). The imaging session lasted for about 6.5 minutes. The relatively slow scan speed was applied in order to increase the SNR and achieve imaging of deeper structures. It can be seen from Fig. 6(a) that imaging of subcutaneous human structures turns more challenging compared to mice as many highly absorbing capillary loops in the dermis (subpapillary plexus) make it difficult to resolve deeper blood vessels. Indeed, the MAP image shown in Fig. 6(c) fails to resolve the subcutaneous vasculature. We therefore applied a virtual skin removal algorithm that eliminates the strong surface signal and thus increases deep tissue contrast. Since it was assumed that the thickness of the epidermis remains approximately constant, the algorithm finds the first maximum in the optoacoustic signal, originating from the stratum corneum, and suppresses signals originating from within a certain range before and after the maximum. By varying this range, images can be optimized to enhance deep tissue vasculature, as shown in Figs. 6(c)–6(f). It must be noted that because it is generally difficult to properly fix the palm in the *in vivo* experiments, motion artifacts might have led to image blurring and overall loss of image quality.
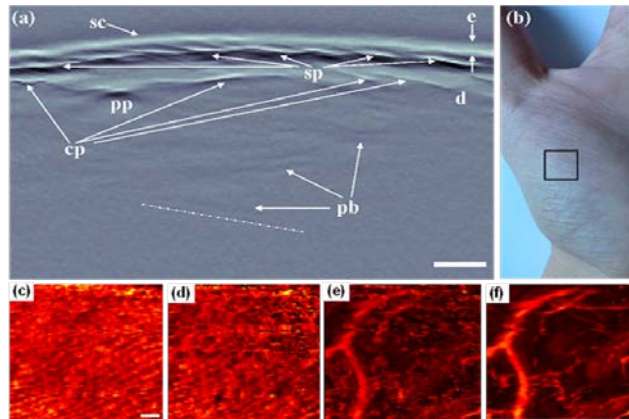
Fig. 6. Imaging of a human palm. (a) 2D optoacoustic imaging of human palm. Above the dot-dash line shows an imaging depth of 3.2 mm; (b) A picture of the imaged palm with black frame indicating the area that was used for later on 3D optoacoustic imaging. Abbreviations: sc - stratum corneum; e - epidermis; d - dermis; sp - subpapillary plexus; pp - princeps pollicis; cp - cutaneous plexus; pb - pollicis brevis. Application of skin removal algorithm for deep tissue contrast enhancement is shown in (c)-(f). MAP optoacoustic image of the entire imaged area without removing signals from the skin is shown in (c). Panels (d)-(f) show the corresponding MAP images after removing signals up to a depths of 330 µm, 420 µm, and 540 µm, respectively. Scale bars: 1mm.

Optoacoustic images acquired from the author's left index finger are shown in Fig. 7(a)–7(d). The system was able to reach the finger bone at a depth of approximately 4.7 mm beneath the stratum corneum layer, as shown in Fig. 7(b). The actual depth and intensity of blood vessels can be of course altered due to speed of sound differences in the nail versus soft tissues.

Figure 7(e) shows an optoacoustic image acquired from the back of the left hand (opisthenar) with the imaged position shown in Fig. 7(f). Signals originating from the skin were removed in order to underline signals from deep tissue. We further applied logarithmic correction in order to compensate for light attenuation and enhance deep tissue contrast, as can be seen in the inset of Fig. 7(e). The deepest resolvable vascular structure in this experiment is located ~6 mm beneath the skin surface (shown with white arrows in Fig. 7(e)).
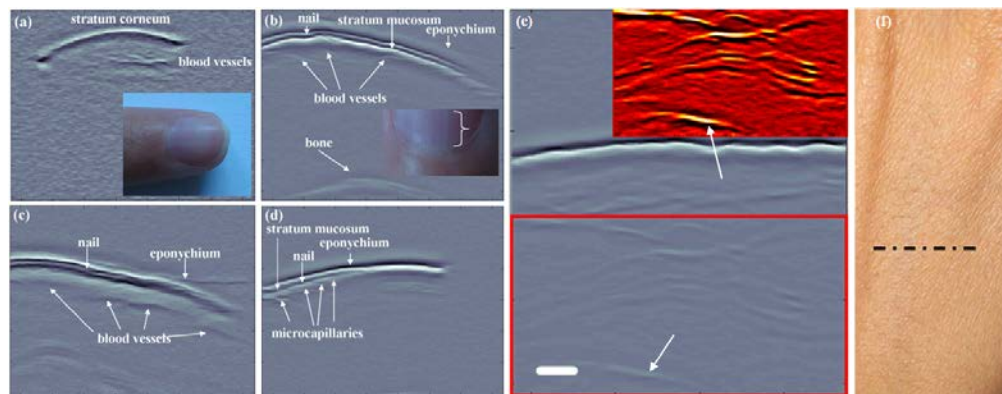

Fig. 7. Optoacoustic images of the author's left index finger at different positions are shown in panels (a)-(d). (e) Optoacoustic image acquired from the back of the left palm (opisthenar). The region tagged with a red-rectangle is enlarged in the inset and presented on a logarithmic scale to enhance contrast from deep tissues; (f) A picture of the left opisthenar. A black dashed line indicates the image location. Scale bar: 1mm.

6. Conclusions

In this paper we demonstrate compact high-resolution optoacoustic microscopy system based on coaxial illumination-detection geometry and a saw-tooth scan motion, which allow real time 2D imaging. The coaxial design allows for optimal coupling of light and increasing the light fluence in the imaged spot, which greatly increases the SNR and helps to reduce out-of-focus artifacts. This, in turn, leads to significantly higher imaging speed and penetration depth of the microscope. In its current implementation the system can acquire five 2D image frames per second with a given lateral scanning range of ~4 mm. However, significantly faster speeds are possible by either increasing the pulse repetition rate of the laser or reducing the scan range. Both phantom and tissue imaging experiments demonstrate good spatial resolution in the range between 11 to 50 µm with an achievable penetration of at least 6 mm into optically dense human tissues. Optimization of the illuminating beam parameters and image reconstruction methodologies are expected to further improve imaging speed, signal to noise ratio and spatial resolution.

A variety of potential pre-clinical and clinical applications may benefit from these new found imaging capabilities. For instance, detection of abnormal capillary shapes and sizes can often address rheumatic diseases and systemic inflammatory diseases [15,16]. Current imaging tools for *in vivo* visualization of nailfold capillaries include nailfold capillaroscopy, which however allows for very shallow penetration, whereas with the aid of our system imaging depth can potentially be significantly extended to get a better insight from deeper vessels surrounding the nailfold. Finally, real time operation greatly assists with reducing motion artifacts, associated with e.g. breathing, heart beat or vascular movements, thus dynamic processes can be visualized with high temporal and spatial resolution. These advantages can be explored in a number of potential applications, such as visualization of deep brain activity.

Acknowledgment